All-Metal Antiaromatic Molecule: Rectangular Al44- in the Li 3Al4- Anion

Aleksey E. Kuznetsov, *et al.*

Science **300**, 622 (2003);
DOI: 10.1126/science.1082477

Science (print ISSN 0036-8075; online ISSN 1095-9203) is published weekly, except the last week in December, by the American Association for the Advancement of Science, 1200 New York Avenue NW, Washington, DC 20005.

1). Changing T in turn affects the well depth and thus T^*, and a transition from the repulsive glass (lower temperatures) to the attractive glass (higher temperatures) is triggered. In Fig. 2B, we see two distinct sets of resolution-limited peaks, with the one for the repulsive glass higher than the one for the attractive glass. Thus, we can conclude that the repulsive glass is better ordered locally than the attractive glass. At $\phi = 0.544$ (Fig. 2C, the A_3 point), we see that the two sharp peaks merge into one sharp peak independent of temperature, signifying that the local structures of the two glasses become identical. Increasing ϕ further to 0.546 (Fig. 2D), the situation remains the same as in the previous volume fraction. This is proof that the MCT predictions are accurate.

Photon correlation spectroscopy was used to investigate the predicted dynamical singularity at the A_3 point. In Fig. 3, intermediate scattering functions (ISFs) measured at $k = 0.00222$ Å^{-1} and at the same four different volume fractions as before are shown as a function of temperature. In Fig. 3A, the ISF measured in an ergodic state exhibits a logarithmic relaxation (indicated by a straight-line fit) at intermediate times followed by a power-law decay before the final α relaxation, in agreement with MCT. The nonergodic state ($T = 300$ K), which has a finite plateau at long times as indicated by the ISF, represents the attractive glass for which the Debye-Waller factor (DWF, the height of the plateau) is about 0.5. Upon increasing ϕ to 0.542 (Fig. 3B), we see that all the ISFs can be grouped into two distinct sets of curves having two different values of DWF: one at 0.5 (attractive glass) and the other at 0.4 (repulsive glass). ISFs in Fig. 3, C and D, indicate that at A_3 and beyond, the DWF of the two glassy states become identical. This is proof of the existence of the A_3 singularity in the phase diagram occurring at exactly the predicted volume fraction. It is, however, worth noting that at A_3 and beyond, the intermediate-time relaxations (the β relaxation region) of the two glassy states are clearly different in spite of the fact that the long-time relaxation becomes identical.

We used photon correlation spectroscopy to verify that the L64/D_2O micellar system follows the phase behavior predicted by MCT with the use of a square well potential with a short-range attraction ($\varepsilon = 0.03$). In particular, we show experimentally the existence of the A_3 singularity in the predicted phase diagram. Our SANS experiment further shows that although the local structures of the attractive and repulsive glasses are in general different, they become identical at the A_3 singularity. It is intriguing to speculate the extent to which one can draw the analogy between the A_3 singularity and the ordinary equilibrium critical point.

References and Notes

1. W. B. Russel, *Colloidal Dispersions* (Cambridge Univ. Press, London, 1992).
2. W. Götze, in *Liquids, Freezing and the Glass Transition*, J. P. Hansen, D. Levesque, J. Zinn-Justin, Eds. (North-Holland, Amsterdam, 1991), part I, pp. 287–503.
3. W. Götze, L. Sjögren, *Rep. Prog. Phys.* **55**, 241 (1992).
4. P. N. Pusey, W. van Megan, *Phys. Rev. Lett.* **59**, 2083 (1987).
5. W. van Megan, P. N. Pusey, *Phys. Rev. A* **43**, 5429 (1991).
6. W. van Megan, S. M. Underwood, *Phys. Rev. E* **49**, 4206 (1994).
7. E. R. Weeks, J. C. Crocker, A. C. Levitt, A. Schofield, D. A. Weitz, *Science* **287**, 627 (2000).
8. E. R. Weeks, D. A. Weitz, *Phys. Rev. Lett.* **89**, 095704 (2002).
9. M. Fuchs, *Transp. Theory Stat. Phys.* **24**, 855 (1995).
10. E. Bartsch, M. Antonietti, W. Schupp, H. Sillescu, *J. Chem. Phys.* **97**, 3950 (1992).
11. T. Eckert, E. Bartsch, *Phys. Rev. Lett.* **89**, 125701 (2002).
12. K. Dawson *et al.*, *Phys. Rev. E* **63**, 011401 (2001).
13. E. Zaccarelli, G. Foffi, K. A. Dawson, F. Sciortino, P. Tartaglia, *Phys. Rev. E* **63**, 031501 (2001).
14. L. Fabbian, W. Götze, F. Sciortino, P. Tartaglia, F. Thiery, *Phys. Rev. E* **59**, R1347 (1999).
15. J. Bergenholtz, M. Fuchs, *Phys. Rev. E* **59**, 5706 (1999).
16. ———, *J. Phys. Condens. Matter* **11**, 10171 (1999).
17. E. Bartsch, T. Eckert, C. Pies, H. Sillescu, *J. Non-Cryst. Solids* **307–310**, 802 (2002).
18. K. N. Pham *et al.*, *Science* **296**, 104 (2002).
19. F. Mallamace *et al.*, *Phys. Rev. Lett.* **84**, 5431 (2000).
20. P. N. Segrè, V. Prasad, A. B. Schofield, D. A. Weitz, *Phys. Rev. Lett.* **86**, 6042 (2001).
21. In a recent study (*28*), we found that within a certain volume fraction range, a reentrant transition from liquid (L) to attractive glass (AG) to liquid to repulsive glass (RG) (i.e., L-AG-L-RG) is observed upon increasing the temperature from 283 to 343 K.
22. W. R. Chen, S. H. Chen, F. Mallamace, *Phys. Rev. E* **66**, 021403 (2002).
23. For example, see E. G. Ponyatovsky, O. I. Barkalov, *Mater. Sci. Rep.* **8**, 147(1992).
24. S. H. Chen, C. Liao, E. Fratini, P. Baglioni, F. Mallamace, *Colloids Surf. A* **95**, 183 (1999).
25. C. Y. Liao, S. M. Choi, F. Mallamace, S. H. Chen, *J. Appl. Crystallogr.* **33**, 677 (2000).
26. L. Lobry, N. Micali, F. Mallamace, C. Liao, S. H. Chen, *Phys. Rev. E* **60**, 7076 (1999).
27. K. W. Zhang, B. Lindman, L. Coppola, *Langmuir* **11**, 538 (1995).
28. W. R. Chen, S. H. Chen, F. Mallamace, in preparation.

29. The research at MIT is supported by a grant from Materials Science Division of U.S. DOE. The research in Messina is supported by INFM-PRA98 and MURST-PRIN2000. We are grateful to C. Glinka of the Center of Neutron Research (National Institute of Standards and Technology) and P. Thiyagarajan of the Intense Pulsed Neutron Source (Argonne National Laboratory) for the beam time of NG7 and SAND spectrometers, respectively, and for their technical assistances.

14 January 2003; accepted 24 March 2003

All-Metal Antiaromatic Molecule: Rectangular Al_4^{4-} in the $Li_3Al_4^-$ Anion

Aleksey E. Kuznetsov,[1] K. Alexander Birch,[1] Alexander I. Boldyrev,[1]* Xi Li,[2,3] Hua-Jin Zhai,[2,3] Lai-Sheng Wang[2,3]*

We report the experimental and theoretical characterization of antiaromaticity in an all-metal system, $Li_3Al_4^-$, which we produced by laser vaporization and studied with the use of photoelectron spectroscopy and ab initio calculations. The most stable structure of $Li_3Al_4^-$ found theoretically contained a rectangular Al_4^{4-} tetraanion stabilized by the three Li^+ ions in a capped octahedral arrangement. Molecular orbital analyses reveal that the rectangular Al_4^{4-} tetraanion has four π electrons, consistent with the $4n$ Hückel rule for antiaromaticity.

The stabilization of aromatic systems (*1*), cyclic systems with $4n + 2$ π electrons, was first understood in organic molecules. On the basis of these ideas, numerous inorganic aromatic molecules have been synthesized and characterized, including all-metal systems (*2–7*). The concept of antiaromaticity, the corresponding destabilization seen in cyclic systems with $4n$ π electrons, was introduced by Breslow (*8, 9*) and is perhaps best understood in cyclobutadiene. However, examples of antiaromatic compounds outside of organic chemistry do not appear to have been reported.

We explored whether an antiaromatic all-metallic compound could be synthesized on the basis of an all-metal aromatic system, Al_4^{2-} (*3*). This molecule, which is stabilized by a counterion such as Li^+, contains two π electrons and assumes a square shape. The reduced species, Al_4^{4-}, would contain four π electrons and would take on a rectangular shape if the two additional electrons entered a π orbital.

We used a laser vaporization source to make such a species stabilized by Li^+ in the form of $Li_3Al_4^-$, and then studied it with anion photoelectron spectroscopy (*10–12*). We made the $Li_3Al_4^-$ clusters with an Al-Li

[1]Department of Chemistry and Biochemistry, Utah State University, Logan, UT 84322, USA. [2]Department of Physics, Washington State University, 2710 University Drive, Richland, WA 99352, USA. [3]W. R. Wiley Environmental Molecular Sciences Laboratory, Pacific Northwest National Laboratory, Mail Stop K8-88, Post Office Box 999, Richland, WA 99352, USA.

*To whom correspondence should be addressed. E-mail: boldyrev@cc.usu.edu, ls.wang@pnl.gov

alloy target and measured its photoelectron spectra at several photon energies (Fig. 1) (*12*). Aluminum and lithium form a strong alloy (AlLi) that makes ideal targets for laser vaporization. The high lithium content in the alloy allows $Li_xAl_y^-$ clusters to be produced with a wide range of Li stoichiometry (*12*). The photoelectron spectra of size-selected $Li_3Al_4^-$ exhibit four major detachment features (*X*, *A*, *B*, and *C*) and three weak features (*a*, *b*, and *c*). The vertical electron detachment energies of these features were measured from the peak maxima (Table 1) and compared to the results of ab initio calculations, as discussed below.

We performed ab initio calculations on a wide variety of structures for $Li_3Al_4^-$ in search of the global minimum using three different theoretical methods (*13, 14*). We found five isomers for the $Li_3Al_4^-$ species lying very close to each other near the energy global minimum (Fig. 2, B to F). At the B3LYP/6-311+G* level of theory (*13*), the most stable structure was the "fork" structure (Fig. 2D). However, at our highest level of theory, CCSD(T)/6-311+G(2df) (*13*), the most stable structure was the capped octahedral singlet structure (Fig. 2B) with the four low-lying isomers in the following order: the capped octahedral triplet structure (Fig. 2C), the "fork" singlet structure (Fig. 2D), the "hood" singlet structure (Fig. 2E), and the "scooter" singlet structure (Fig. 2F). Numerous other isomers were also located for $Li_3Al_4^-$ (fig. S1), but at all levels of theory they have higher energies than the five low-lying structures shown in Fig. 2. The ground state of $Li_3Al_4^-$ indeed has a rectangular Al_4 framework; the distortion from a perfect rectangular Al_4 is caused by the asymmetric capping of the third Li atom. We calculated the structure of the neutral Li_4Al_4 cluster (Fig. 2A) and found that it indeed contains an ideal rectangular Al_4 framework, as expected. This cluster has been studied with molecular dynamics within the framework of density functional theory (*15*). A similar capped octahedron was obtained, but the four Al atoms were shown to form a rhombus, unlike the current results, where Al atoms form a perfect rectangular framework.

To facilitate comparisons with the experimental data, we further calculated the low-lying vertical detachment energies for the five $Li_3Al_4^-$ isomers (Table 1). We obtained an excellent agreement between the first five vertical detachment channels calculated for the ground-state structure (Fig. 2B) and the four major experimental peaks (*X*, *A*, *B*, and *C*). The calculated detachment energies from the 3a′ and 2a″ orbitals are very close and should correspond to the band *C*, which is relatively broad (Fig. 1). Ab initio calculations predict that there are no one-electron detachment channels between 3.0 and 6.3 eV, consistent with the absence of any major peaks beyond 3 eV in the $Li_3Al_4^-$ spectrum at 193 nm (Fig. 1B). The other three low-lying singlet isomers all have a major transition between 3.5 and 4.5 eV (Table 1) and thus can be excluded from being the contributors to the major observed spectral features. However, there are minor features (*a*, *b*, and *c*) in the spectra of $Li_3Al_4^-$, seen more clearly at 355 nm (Fig. 1A), that could be attributable to impurities or to isomers of $Li_3Al_4^-$. We could rule out contributions from impurities because the mass selection was quite

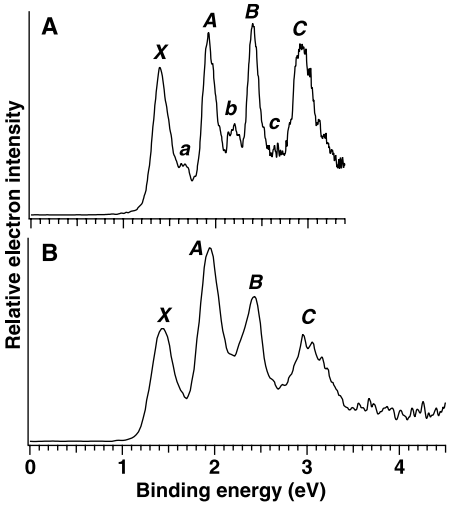

Fig. 1. Photoelectron spectra of $Li_3Al_4^-$ (**A**) at 355 nm (3.496 eV), (**B**) at 193 nm (6.424 eV). The vertical detachment energies for the four major detachment features (*X*, *A*, *B*, *C*) are given in Table 1.

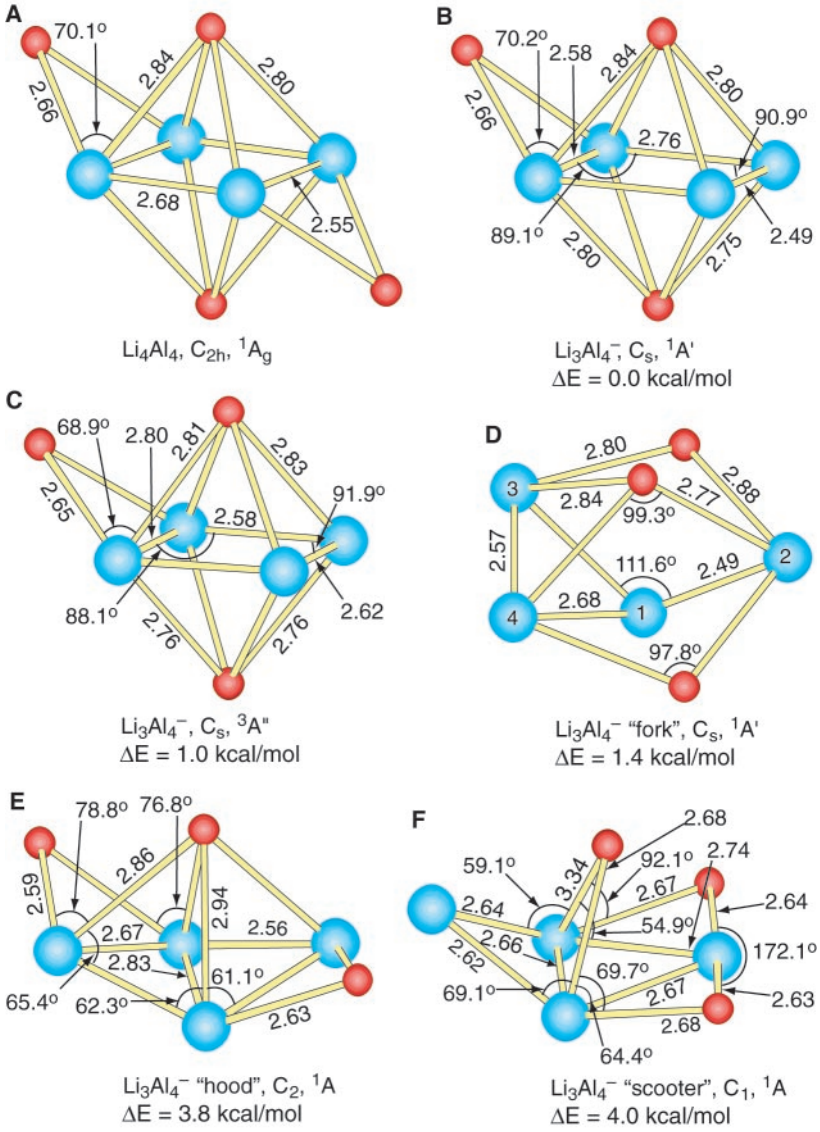

Fig. 2. Optimized structures of Li_4Al_4 and $Li_3Al_4^-$; bond lengths in angstroms. (**A**) Li_4Al_4. (**B**) Capped octahedral singlet $Li_3Al_4^-$ (C_s, $^1A'$). (**C**) Capped octahedral triplet $Li_3Al_4^-$ (C_s, $^3A''$). (**D**) "Fork" $Li_3Al_4^-$ (C_s, $^1A'$). (**E**) "Hood" $Li_3Al_4^-$ (C_2, ^1A). (**F**) "Scooter" $Li_3Al_4^-$ (C_1, ^1A). The structural parameters, given in Å and degrees, are at the B3LYP/6-311+G* level of theory. The relative energies for the isomers of $Li_3Al_4^-$ are at the CCSD(T)/6-311+G(2df) level of theory (*13*).

Table 1. Experimental (exp) vertical electron detachment energies (VDE) in eV of $Li_3Al_4^-$, compared to calculated (theo) VDEs for the ground state and four low-lying isomers of $Li_3Al_4^-$. All energies are in eV.

Experimental peak	VDE (exp)	C_s, $^1A'$, capped octahedron	C_s, $^3A''$, capped octahedron	C_s, $^1A'$, "fork"	C_2, ^1A, "hood"	C_1, ^1A, "scooter"
		MO VDE (theo)*	MO VDE (theo)†	MO VDE (theo)*	MO VDE (theo)*	MO VDE (theo)*
X	1.39 ± 0.07	6a′ 1.34 (0.86)	3a″ 1.21 (0.89) 6a′ 1.34 (0.90)	6a′ 1.66 (0.85)	3b 1.40 (0.86)	8a 1.37 (0.85)
A	1.92 ± 0.06	5a′ 1.85 (0.85)	5a′ 1.66 (0.88) 4a′ 1.90 (0.88)	5a′ 1.88 (0.85)	5a 1.66 (0.85)	7a 2.00 (0.85)
B	2.39 ± 0.05	4a′ 2.39 (0.84)	3a′ 2.18 (0.87)	2a″ 2.15 (0.84)	4a 2.21 (0.84)	6a 2.08 (0.84)
C	2.91 ± 0.08	3a′ 2.92 (0.83) 2a″ 2.96 (0.82) 1a″ 6.32 (−0.01)	2a″ 2.61 (0.86)	4a′ 2.56 (0.84) 3a′ 4.10 (0.79)	3a 2.52 (0.84) 2a 3.53 (0.77)	5a 2.47 (0.84) 4a 3.69 (0.75)

These VDEs were calculated at the ROVGF/6-311+G(2df)//B3LYP/6-311+G level of theory. The numbers in the parentheses indicate the pole strength, which characterizes the validity of the one-electron detachment picture. †These VDEs were calculated at the UOVGF/6-311+G*//B3LYP/6-311+G* level of theory.

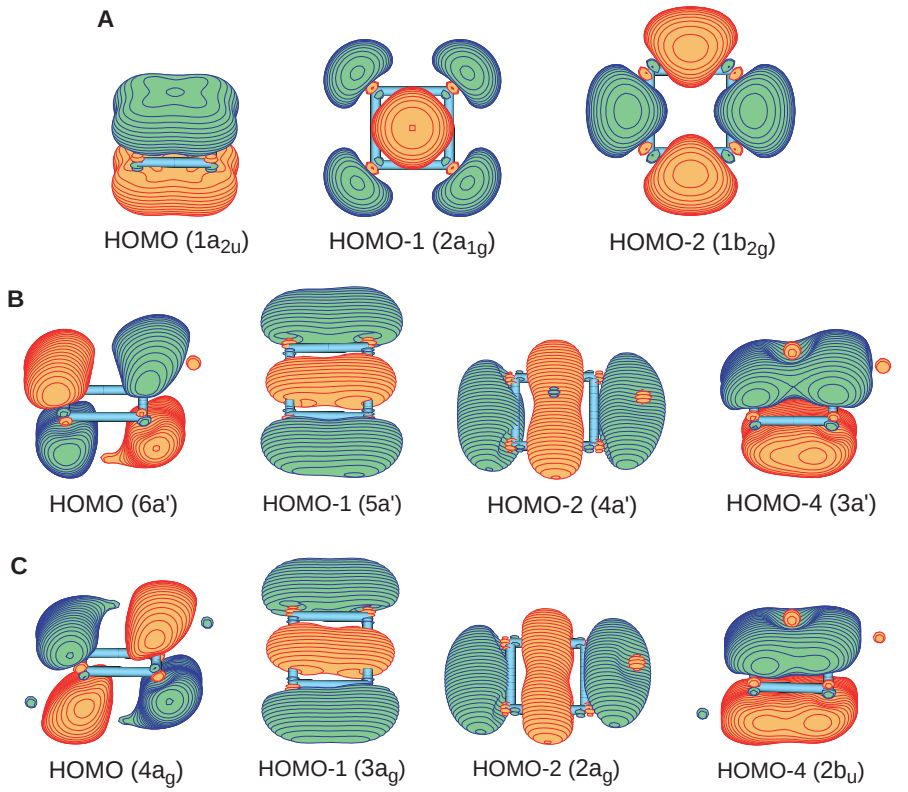

Fig. 3. Molecular orbital pictures. (**A**) Al_4^{2-} (D_{4h}, $^1A_{1g}$); (**B**) capped octahedral singlet $Li_3Al_4^-$ (C_s, $^1A'$); (**C**) Li_4Al_4 (C_{2h}, ^1A_g).

clean. Thus, the minor peaks are most likely due to the presence of minor isomers of $Li_3Al_4^-$, consistent with the theoretical predictions. The best agreement for these minor peaks was found for the "fork" isomer (Table 1), which is the lowest-lying singlet isomer. Contributions from the two other singlet isomers (Fig. 2, E and F) are expected to be small as a result of their higher relative energies (*16*).

The rectangular framework of the Al_4 fragment in $Li_3Al_4^-$ and Li_4Al_4 already hints the presence of antiaromaticity. To provide further evidence, we need to analyze their molecular orbitals (MOs) and see whether they have four π electrons, as shown in Fig. 3 (*17*). For comparison, we also present MOs of Al_4^{2-} (Fig. 3A), which was previously shown to be a 2π electron aromatic system (*3*). The highest occupied MO (HOMO) of Al_4^{2-} (Fig. 3A) is a completely delocalized π orbital ($1a_{2u}$). It also has two delocalized σ MOs: the HOMO-1 ($2a_{1g}$), composed of radial *p*-orbitals, and the HOMO-2 ($1b_{2g}$), composed of perpendicular *p*-orbitals. There are no other bonding MOs in Al_4^{2-}, and the two pairs of σ electrons must be shared by the four Al-Al bonds, giving a σ bond order of 0.5. Thus, the Al_4^{2-} dianion can be considered as π-aromatic and doubly σ-aromatic (*3*–*7*).

The MOs of $Li_3Al_4^-$ and Li_4Al_4 are nearly identical, even though the Al_4 framework in $Li_3Al_4^-$ is slightly distorted from a perfect rectangle as a result of the asymmetric capping by the Li atoms. The Li atoms retain very little charge density, and the two clusters can be viewed as $Li^+{}_3Al_4{}^{4-}$ and $Li^+{}_4Al_4{}^{4-}$. MOs similar to Al_4^{2-} can be seen in $Al_4{}^{4-}$: The completely delocalized π MO (HOMO-4) is considerably stabilized in $Al_4{}^{4-}$, and the two delocalized σ MOs (HOMO-1 and HOMO-2) correspond to the same set in Al_4^{2-} (Fig. 3A). The extra pair of electrons enters the HOMO of $Al_4{}^{4-}$, which is indeed a π MO. This π HOMO of $Al_4{}^{4-}$ is bonding within the two shorter Al-Al bonds but is antibonding between the two pairs of Al atoms (Fig. 3B), resulting in the rectangular shape and antiaromatic character of $Al_4{}^{4-}$. Both the π bonding patterns and the rectangular shape of $Al_4{}^{4-}$ are analogous to the prototypical antiaromatic organic molecule cyclobutadiene, lending considerable credence for it to be an all-metal antiaromatic species. Furthermore, the two delocalized σ-bonding MOs in $Al_4{}^{4-}$ also give it characteristics of σ-aromaticity (*18*).

The introduction of antiaromaticity helps us to understand and characterize the structure and chemical bonding of $Li_3Al_4^-$ and completes the extension of two important chemical concepts, aromaticity and antiaromaticity, into the realm of all-metal systems. We believe that further advancement of the aromaticity and antiaromaticity concepts into metal territory will be of value in understanding not only the properties of metal clusters but also those of bulk metallic and alloy systems.

References and Notes

1. Special issue on Aromaticity, *Chem. Rev.* **101** (no. 5) (2001).
2. For examples, see (*3*–*7*).
3. X. Li, A. E. Kuznetsov, H.-F. Zhang, A. I. Boldyrev, L. S. Wang, *Science* **291**, 859 (2001).
4. A. E. Kuznetsov, J. D. Corbett, L. S. Wang, A. I. Boldyrev, *Angew. Chem. Int. Ed.* **40**, 3369 (2001).
5. P. W. Fowler, R. W. A. Havenith, E. Steiner, *Chem. Phys. Lett.* **342**, 85 (2001).
6. J. Jusélius, M. Straka, D. Sundholm, *J. Phys. Chem. A* **105**, 9939 (2001).
7. C.-G. Zhan, F. Zheng, D. A. Dixon, *J. Am. Chem. Soc.* **124**, 14795 (2002).
8. R. Breslow, W. Chu, *J. Am. Chem. Soc.* **92**, 2165 (1970).
9. R. Breslow, *Acc. Chem. Res.* **6**, 393 (1973).

10. L. S. Wang, H. S. Cheng, J. Fan, *J. Chem. Phys.* **102**, 9480 (1995).
11. L. S. Wang, H. Wu, in *Advances in Metal and Semiconductor Clusters. IV. Cluster Materials*, M. A. Duncan, Ed. (JAI Press, Greenwich, CT, 1998), pp. 299–343.
12. The $Li_3Al_4^-$ species were produced using a laser vaporization supersonic cluster source and an Al-Li alloy target. A wide range of $Li_xAl_y^-$ anionic clusters was produced and analyzed with a time-of-flight mass spectrometer. The $Li_3Al_4^-$ anions of interest were selected for photodetachment in each experiment. Photoelectron spectra were taken at two detachment laser wavelengths, 355 and 193 nm, and were calibrated using the known spectra of Cu^-. The photoelectron energy resolution was about 25 meV for 1-eV electrons.
13. We initially optimized geometries and calculated frequencies of $Li_3Al_4^-$ using analytical gradients with polarized split-valence basis sets (6-311+G*) and a hybrid method known in the literature as B3LYP. The energies of the most stable structures were refined using the coupled-cluster method with single, double, and noniterative triple excitations [CCSD(T)] and the most extended 6-311+G(2df) basis sets. The vertical electron detachment energies were calculated using the outer valence Green Function method [OVGF/6-311+G(2df)] and the B3LYP/6-311+G* geometries for $Li_3Al_4^-$. Core electrons were kept frozen in treating the electron correlations at the CCSD(T) and OVGF levels of theory. All calculations were performed using the Gaussian 98 program on a 63-nodes Birch-Retford Beowulf cluster computer built at Utah State by K. A. Birch and B. P. Retford.
14. M. J. Frisch *et al*., *Gaussian 98* (revision A.7), Gaussian Inc., Pittsburgh, PA (1998).
15. S. Chasko, M. Desphande, D. G. Kanhere, *Phys. Rev. B* **64**, 155409 (2001).
16. We did not observe much contribution from the triplet capped octahedron structure, whose first vertical detachment energy is rather low (Table 1). It may be that the triplet isomer is actually higher in energy than we estimated from our calculations. The expansion of one-electron basis sets and inclusion of higher orders in the coupled cluster theory usually increase stability of the singlet state over the corresponding triplet state.
17. The MO pictures were made with the MOLDEN3.4 program (G. Schaftenaar, MOLDEN3.4, CAOS/CAMM Center, Netherlands, 1998).
18. The calculated molecular properties of other low-lying isomers are given in tables S1 to S5.
19. The theoretical work done at Utah was supported by the donors of the Petroleum Research Fund, administered by the American Chemical Society. The experimental work done at Washington was supported by the National Science Foundation. The experiment was performed at the W. R. Wiley Environmental Molecular Sciences Laboratory, a national scientific user facility sponsored by the Office of Biological and Environmental Research of the U.S. Department of Energy (DOE) and located at Pacific Northwest National Laboratory, which is operated for DOE by Battelle.

Supporting Online Material

www.sciencemag.org/cgi/content/full/300/5619/622/DC1
Fig. S1
Tables S1 to S5

17 January 2003; accepted 17 March 2003

Casting Metal Nanowires Within Discrete Self-Assembled Peptide Nanotubes

Meital Reches and Ehud Gazit*

Tubular nanostructures are suggested to have a wide range of applications in nanotechnology. We report our observation of the self-assembly of a very short peptide, the Alzheimer's β-amyloid diphenylalanine structural motif, into discrete and stiff nanotubes. Reduction of ionic silver within the nanotubes, followed by enzymatic degradation of the peptide backbone, resulted in the production of discrete nanowires with a long persistence length. The same dipeptide building block, made of D-phenylalanine, resulted in the production of enzymatically stable nanotubes.

Self-assembled nanostructures provide a key direction for the controlled fabrication of novel nanoscopic materials and devices. Nanotubular structures are particularly important structural elements because they may serve as nanowires or nanoscaffolds (*1–4*). Peptide nanotubes are especially intriguing assemblies because they have the scope for numerous chemical modifications and allow the use of biological systems specificity. A milestone in the production of peptide-based nanotubes was the demonstration by Ghadiri *et al.* (*2*, *5*) that a cyclic octapeptide with alternating L and D amino acids can form a nanotubular structure by self-assembly. However, the peptide nanotubes that formed further assembled into an array of tubes that were aligned as crystalline microscopic structures (*2*, *5*). Linear surfactant-like hepta- and octapeptides can also self-assemble into a network of open-ended nanotubes, from which nanovesicles can "bud" or "fuse" (*3*, *4*). Peptide-related bis(*N*-α-amido-glycylglycine)-1,7-heptane dicarboxylate molecules were also shown to be assembled into tubular structures (*6*).

We observed the formation of peptide nanotubes while studying the ability of very short aromatic peptides (hexapeptides and shorter) to form well-ordered amyloid fibrils (*7–9*). Amyloid fibrils are the hallmark of a diverse group of diseases of unrelated origin, including Alzheimer's disease, type II diabetes, and prion diseases (*10–15*). Despite their formation by a diverse and structurally unrelated group of proteins, all amyloid fibrils share similar biophysical and structural properties. On the basis of both experiments and theory, we recently suggested that stacking of aromatic residues may play a key role in the process of molecular recognition and self-assembly that leads to the formation of amyloid fibrils (*16*). This proposal is in agreement with the well-known role of aromatic stacking in the formation of chemical and biochemical supramolecular structures (*17–19*). According to our suggestion, the restricted geometry and the attractive forces of the aromatic moieties provide order and directionality as well as the energetic contribution needed for the formation of such well-ordered structures. In this context, we were intrigued to determine the molecular properties of a peptide fragment corresponding to the core recognition motif of Aβ, the diphenylalanine element (Fig. 1A). This motif is of special interest, because several studies have identified the ability of larger peptides and conjugated organic molecules that contain this motif to inhibit fibril formation by Aβ (*20–22*). Some of those inhibitors are currently undergoing clinical trials as potential drugs to treat Alzheimer's disease (*23*, *24*).

Here, we sought to make the NH_2-Phe-Phe-COOH dipeptide soluble at very high concentrations (≥100 mg/ml) by dissolving the lyophilized peptide in 1,1,1,3,3,3 hexafluoro-2-propanol. Although the peptide appeared to be highly soluble in the organic solvent, a rapid assembly into ordered semi-crystalline structures was observed visually within seconds after dilution into the aqueous solution at a final μM concentration range. We used dynamic light scattering analysis to determine assembly into supramolecular structures within minutes at the μM range. Transmission electron microscopy (TEM) analysis with negative staining indicated that the peptide forms well-ordered, tubular, and elongated assemblies (Fig. 1B). The light shell and the dark center, as observed in Fig. 1B, suggested hollow tubular structures filled with the negative stain, uranyl acetate. Energy-dispersive x-ray analysis (EDX) indicated the presence of uranium within the assembled structures (fig. S1A). Smaller structures could also be observed by TEM analysis; we propose that these represent smaller tubular assemblies or fragments of the larger nanotubes. The persistence length of the nanotubes appears to be on the order of microme-

Department of Molecular Microbiology and Biotechnology, George S. Wise Faculty of Life Sciences, Tel Aviv University, Tel Aviv 69978, Israel.

*To whom correspondence should be addressed. E-mail: ehudg@post.tau.ac.il